

Experimental studies of H_2/Ar plasma in a cylindrical inductive discharge with an expansion region

Shi-Bo Li(李世博), Si-Yu Xing(邢思雨), Fei Gao(高飞), and You-Nian Wang(王友年)

Citation: Chin. Phys. B, 2024, 33 (**10**): 105201. DOI: 10.1088/1674-1056/ad6250
Journal homepage: http://cpb.iphy.ac.cn; http://iopscience.iop.org/cpb

What follows is a list of articles you may be interested in

Power transfer efficiency in an air-breathing radio frequency ion thruster

Gao-Huang Huang(黄高煌), Hong Li(李宏), Fei Gao(高飞), and You-Nian Wang(王友年)
Chin. Phys. B, 2024, 33 (**7**): 075201. DOI: 10.1088/1674-1056/ad426c

Fundamental study towards a better understanding of low pressure radio-frequency plasmas for industrial applications

Yong-Xin Liu(刘永新), Quan-Zhi Zhang(张权治), Kai Zhao(赵凯), Yu-Ru Zhang(张钰如), Fei Gao(高飞),Yuan-Hong Song(宋远红), and You-Nian Wang(王友年)
Chin. Phys. B, 2022, 31 (**8**): 085202. DOI: 10.1088/1674-1056/ac7551

Numerical investigation of radio-frequency negative hydrogen ion sources by a three-dimensional fluid model

Ying-Jie Wang(王英杰), Jia-Wei Huang(黄佳伟), Quan-Zhi Zhang(张权治), Yu-Ru Zhang(张钰如), Fei Gao(高飞), and You-Nian Wang(王友年)
Chin. Phys. B, 2021, 30 (**9**): 095205. DOI: 10.1088/1674-1056/ac0e21

Time-resolved radial uniformity of pulse-modulated inductively coupled O_2/Ar plasmas

Wei Liu(刘巍), Chan Xue(薛婵), Fei Gao(高飞), Yong-Xin Liu(刘永新), You-Nian Wang(王友年), and Yong-Tao Zhao(赵永涛)
Chin. Phys. B, 2021, 30 (**6**): 065202. DOI: 10.1088/1674-1056/abe3f5

Numerical simulation and experimental validation of multiphysics field coupling mechanisms for a high power ICP wind tunnel

Ming-Hao Yu(喻明浩), Zhe Wang(王哲), Ze-Yang Qiu(邱泽洋), Bo Lv(吕博), and Bo-Rui Zheng(郑博睿)
Chin. Phys. B, 2021, 30 (**6**): 065201. DOI: 10.1088/1674-1056/abeb0e

---

Experimental studies of H_2/Ar plasma in a cylindrical inductive discharge with an expansion region

Shi-Bo Li(李世博), Si-Yu Xing(邢思雨), Fei Gao(高飞)†, and You-Nian Wang(王友年)

Key Laboratory of Materials Modification by Laser, Ion, and Electron Beams (Ministry of Education), School of Physics, Dalian University of Technology, Dalian 116024, *China*

(Received 7 May 2024; revised manuscript received 20 June 2024; accepted manuscript online 12 July 2024)

The electrical parameters of H_2/Ar plasma in a cylindrical inductive discharge with an expansion region are investigated by a Langmuir probe, where Ar fractions range from 0% to 100%. The influence of gas composition and pressure on electron density, the effective electron temperature and the electron energy probability functions (EEPFs) at different spatial positions are present. In driver region, with the introduction of a small amount of Ar at 0.3 Pa, there is a rapid increase in electron density accompanied by a decrease in the effective electron temperature. Additionally, the shape of the EEPF transitions from a three-temperature distribution to a bi-Maxwellian distribution due to an increase in electron–electron collision. However, this phenomenon resulting from the changes in gas composition vanishes at 5 Pa due to the prior depletion of energetic electrons caused by the increase in pressure during hydrogen discharge. The EEPFs for the total energy in expansion region is coincident to these in the driver region at 0.3 Pa, as do the patterns of electron density variation between these two regions for differing Ar fractions. At 5 Pa, as the discharge transitions from H_2 to Ar, the EEPFs evolved from a bi-Maxwellian distribution with pronounced low energy electrons to a Maxwellian distribution in expansion region. This evolve may be attributed to a reduction in molecular vibrational excitation reactions of electrons during transport and the transition from localized electron dynamics in hydrogen discharge to non-localized electron dynamics in argon discharge. In order to validate the experimental results, we use the COMSOL simulation software to calculate electrical parameters under the same conditions. The evolution and spatial distribution of the electrical parameters of the simulation results agree well with the trend of the experimental results.

Keywords: inductively coupled plasma, transmission and distribution, energy distribution functions

PACS: 52.25.–b, 52.25.Fi, 52.50.–b **DOI:** 10.1088/1674-1056/ad6250

1. Introduction

H_2-containing plasmas have a variety of applications, such as semiconductor-device fabrication processes, material processing and nuclear-fusion operation.[1–14] In particular, H_2/Ar mixtures are of interest for hydrogenation of transistors and the production of silicon based photovoltaic cells.[15–23] The species that play a major role in H_2/Ar mixed plasma in process treatment are mainly ions, reactive hydrogen atoms, metastable Ar atoms, and high-energy photons.

There has been a great deal of research on the characterizing plasma properties in H_2/Ar discharge. Gudmundsson[24,25] studied the plasma parameters in a low pressure (20 mTorr, 40 mTorr, and 60 mTorr, 1 Torr = 1.33322×10^2 Pa) planar inductively coupled H_2/Ar discharge using a Langmuir probe and a mass spectrometer at 13.56 MHz. This work shows that the electron density increases with increasing fractional Ar pressure, and the ion energy distributions and uncorrected flux ratios of most ion types present (H^+, H_2^+, H_3^+, and Ar^+) are also given. Kimura and Kasugai[26] studied the H_2/Ar mixed discharge by a Langmuir probe and an emission spectroscopy, and verified the results with a global model in a planar inductively coupled discharge. They estimated the effective ion mass through the ion current collected into the probe, and found that H_3^+ can replace Ar^+ as the dominant positive ion at Ar proportions above 80%–85%. Experimental results are in reasonably good agreement with the global model results, and the global model results show that the most ion types present should include ArH^+. Hjartarson *et al.*[27] investigated a global model for H_2/Ar discharge, in which the presence of H^- ions and vibrational hydrogen molecules was considered. It was found that ArH^+ has a crucial effect on the destruction of the H^- ion. Sode *et al.*[28] comprehensive showed the variation of experimental parameters with different H_2/Ar mixing ratios in a planar inductively coupled discharge at 1 Pa using various diagnostic methods. They first obtained the absolute ion densities through an energy-dispersive mass spectrometer and the developed calibration program, and one of the results is that the predominant ion species is the ArH^+ ion in mixed H_2/Ar plasmas (the Ar fraction is 12.6%–72.3%), accounting for approximately 2/3 of total ion density. Subsequently, Sode *et al.*[29] devised a rate equation model to investigate the ion composition of H_2/Ar plasmas. They discussed the production and loss channels of all ions, and pointed out that the higher density of ArH^+ is caused by the lower wall loss compared with hydrogen ions. Fox-Lyon *et al.*[30] obtained Ar metastable atom densities using a model combining

†Corresponding author. E-mail: fgao@dlut.edu.cn

© 2024 Chinese Physical Society and IOP Publishing Ltd

electrical and optical plasma characterization data, and found that the density of Ar metastable atom increases with increasing fractional Ar pressure. Then, Fox-Lyon *et al.*[31] studied the effects of isotopes on plasma species of the Ar/H_2/D_2 discharge. They found that electrical characteristics of H_2/Ar and D_2/Ar are similar, D_2 has more molecular ions due to the larger collision cross-section with Ar^+ ions and the slower loss of D-containing molecular ions at wall, the D_2/Ar plasma has a higher etching rate for hydrocarbons.

Indeed, the EEPF is an important parameter for understanding the physical properties of inductively coupled plasma (ICP), as it directly affects the rate coefficients of electron impact reaction, such as ionization rate, excitation rate, thus affecting plasma components. Huh[32] and Yang[33] *et al.* developed a global model with an arbitrary EEPF to investigate a low pressure inductively coupled hydrogen plasma. They found that the results under assuming the bi-Maxwellian EEPF achieves a higher H^- ion density at low pressure compared to the Maxwellian EEPF. The presence of high-energy electrons in bi-Maxwellian EEPF leads to higher electron impact collision reaction rate constants for the vibrational excitation and other reactions. Additionally, the plasma with a bi-Maxwellian EEPF exhibits a higher electron density, which promotes H^- precursor production. The EEPF in ICP is influenced by various factors, including the gas type, RF (radio-frequency) power, and gas pressure. Additionally, for large single- or two-chamber configurations, it is also important to consider the spatial transport phenomena within the plasma. Gao *et al.*[34] experimentally studied plasma parameters in inductively coupled hydrogen discharges with an expansion region, and they revealed that the EEPF in the driver region is bi-Maxwellian shape, which is converted to the Maxwellian shape in the expansion region at low pressure.

Although many efforts have been carried out in H_2/Ar plasma, the emphasis is mainly focus on the evolution of particle composition with H_2/Ar mixing ratios at a fixed position in planar-coil discharge without providing information about the spatial dependence of the plasma parameter. However, this information is necessary to understand the complex physics related to spatial transport in large geometric dimension chamber systems, especially in two-chamber systems. Therefore, the objectives of this work are to investigate the parameters at different spatial positions in a cylindrical coil inductively coupled H_2/Ar discharge with an expansion region.

The paper is organized as follows. In Section 2, the present of experimental device is given, and a fluid model is described in Section 3. In Section 4, the effect of gas ratio and pressure on plasma parameters at specific positions in two-chamber H_2/Ar ICP are present, and the corresponding phenomena are discussed. Finally, the conclusions are presented in Section 5.

2. Experimental setup

The schematic diagram of setup is shown in Fig. 1. The discharge driver chamber is composed of a quartz cylinder with 8 turns of water-cooled copper coil wound externally to generate the plasma, which is 12 cm in diameter and 14 cm in height. One end of the coil is connected to a 2-MHz RF power via a Γ-type matching networking and the other is grounded. The forward power is fixed at 2 kW, and monitored by a VI-probe placed in front of the matching networking. The discharge expansion chamber is a stainless steel cylinder with an inner diameter of 30 cm and a height of 40 cm. The pumping system composing of a mechanical pump (500 L/min) and a turbine molecular pump (1200 L/s) connected to the bottom of the expansion chamber through vacuum piping, and the background pressure is of the order of 10^{-4} Pa. The working gas components are controlled by two mass-flow controllers, and the total flow rate (equals to the sum of the two flow rates) is maintained at about 7 sccm. A detailed description of the device can be found in our previous articles.[34–37]

A commercial Langmuir probe system is used to measure plasma *I*–*V* curves with a probe tip made of tungsten wire with 0.2 mm in diameter and 8 mm in length. The probe is installed axially along the reactor through the flange at the bottom of the expansion chamber. With the top of the driver chamber as the origin, it can be moved along the axial direction in the range of 0 cm–30 cm, and we choose the $z = 6$ cm and the $z = 24$ cm as representative locations for the driver region and the expansion region, as the former is the center of the driver region, and the latter is near the center of the expansion region within the measurable range. The EEPF is obtained from the second derivative of the *I*–*V* curves, and the formula is as follows:[38]

$$f(\varepsilon) = \frac{(8m_e)^{1/2}}{e^{3/2}A_p}\frac{\mathrm{d}^2 I}{\mathrm{d}V^2}, \tag{1}$$

where $\varepsilon = \frac{1}{2}m_e v^2/e$, v is electron electronic speed, m_e is electron mass, e is the electron charge, A_p is the probe area, I is the electron current collected by the probe, and V is the voltage difference between the plasma potential and the probe sweep voltage. The plasma potential can be obtained from the voltage value corresponding to the zero-point of the second derivative in the *I*–*V* curve obtained from the probe.

The electron density and the effective electron temperature are calculated using the measured EEPF

$$n_e = \int_0^\infty \varepsilon^{1/2} f(\varepsilon)\,\mathrm{d}\varepsilon, \tag{2}$$

$$T_{\mathrm{eff}} = \frac{2}{3n_e}\int_0^\infty \varepsilon^{3/2} f(\varepsilon)\,\mathrm{d}\varepsilon, \tag{3}$$

where ε is the electron kinetic energy.

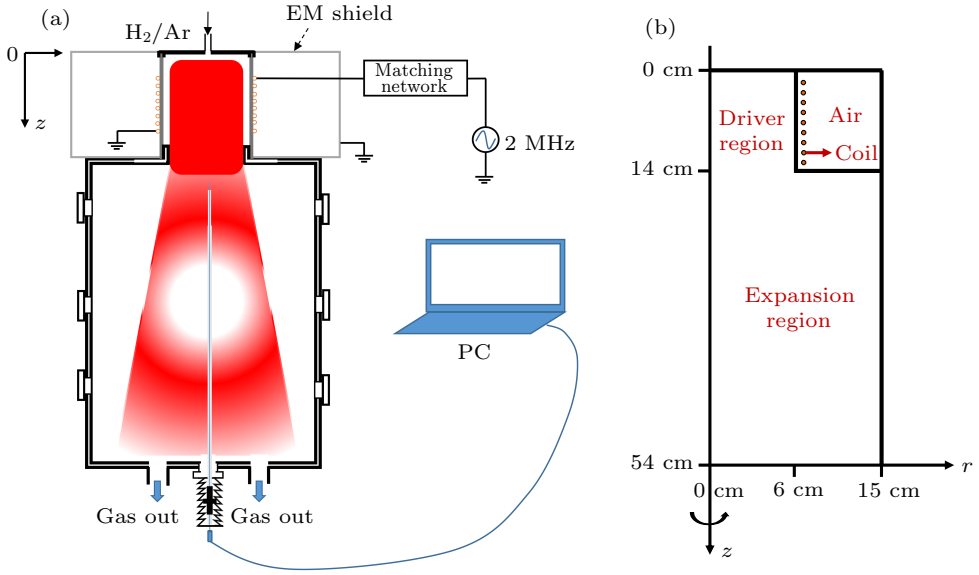


Fig. 1. Schematic diagram of the experimental apparatus (a) and simulation domain (b).

3. Model setup

As shown in Fig. 1(b), the simulation area has the same dimensions as the experimental chamber and a two-dimensional (2D) axisymmetric fluid model is built using COMSOL Multiphysics. The model contains a plasma module and a magnetic field module. The plasma module includes the continuity, drift-diffusion, energy conservation, and Poisson's equations. The continuity equation and the drift-diffusion equation are used to solve for the densities and fluxes of various particles

$$\frac{\partial n_{\mathrm{e}}}{\partial t}+\nabla\cdot\boldsymbol{\Gamma}_{\mathrm{e}}=R_{\mathrm{e}}, \tag{4}$$

$$\boldsymbol{\Gamma}_{\mathrm{e}}=-n_{\mathrm{e}}\mu_{\mathrm{e}}\boldsymbol{E}_0-D_{\mathrm{e}}\nabla n_{\mathrm{e}}, \tag{5}$$

$$\frac{\partial n_{\mathrm{i}}}{\partial t}+\nabla\cdot\boldsymbol{\Gamma}_{\mathrm{i}}=R_{\mathrm{i}}, \tag{6}$$

$$\boldsymbol{\Gamma}_{\mathrm{i}}=-n_{\mathrm{i}}\mu_{\mathrm{i}}\boldsymbol{E}_0-D_{\mathrm{i}}\nabla n_{\mathrm{i}}, \tag{7}$$

$$\frac{\partial n_{\mathrm{k}}}{\partial t}+\nabla\cdot\boldsymbol{\Gamma}_{\mathrm{k}}=R_{\mathrm{k}}, \tag{8}$$

$$\boldsymbol{\Gamma}_{\mathrm{k}}=-n_{\mathrm{k}}\mu_{\mathrm{k}}\boldsymbol{E}_0-D_{\mathrm{k}}\nabla n_{\mathrm{k}}, \tag{9}$$

where $n_{\mathrm{e}}(\boldsymbol{\Gamma}_{\mathrm{e}})$, $n_{\mathrm{i}}(\boldsymbol{\Gamma}_{\mathrm{i}})$, and $n_{\mathrm{k}}(\boldsymbol{\Gamma}_{\mathrm{k}})$ are the electron, ion, and neutral particle densities (fluxes), respectively. $\boldsymbol{E}_0$ is the electrostatic field generated by charge separation. $\mu_{\mathrm{e}}(D_{\mathrm{e}})$, $\mu_{\mathrm{i}}(D_{\mathrm{i}})$, and $\mu_{\mathrm{k}}(D_{\mathrm{k}})$ are the mobility (diffusion coefficient) of the various particles, respectively. R_{k} is the source term.

For ions the temperature is set to a constant value of 300 K, so the energy conservation equation is only used to solve the temperature of the electron

$$\frac{\partial}{\partial t}\left(\frac{3}{2}n_{\mathrm{e}}T_{\mathrm{e}}\right)+\nabla\cdot\boldsymbol{Q}_{\mathrm{e}}+e\boldsymbol{\Gamma}_{\mathrm{e}}\cdot\boldsymbol{E}_0=P_{\mathrm{abs}}-R_{\mathrm{en}}, \tag{10}$$

where T_{e} is the electron temperature and e is the elementary charge. $\boldsymbol{Q}_{\mathrm{e}}$ is the electron energy flux, P_{abs} is the inductive power deposition density and R_{en} is the electron energy loss due to inelastic collisions.

The boundary conditions for electron flux and electron energy flux in the plasma region are as follows:

$$\boldsymbol{n}\cdot\boldsymbol{\Gamma}_{\mathrm{e}}=\frac{1}{4}(1-r_{\mathrm{e}})n_{\mathrm{e}}v_{\mathrm{th}}, \tag{11}$$

$$\boldsymbol{n}\cdot\boldsymbol{Q}_{\mathrm{e}}=\frac{5}{2}T_{\mathrm{e}}(\boldsymbol{n}\cdot\boldsymbol{\Gamma}_{\mathrm{e}}), \tag{12}$$

where $\boldsymbol{n}$ is the elementary surface vector, r_{e} is the reflection coefficient on the vessel wall, and v_{th} is the electron thermal velocity. The boundary conditions for the ion flux and the neutral particle flux are

$$\boldsymbol{n}\cdot\boldsymbol{\Gamma}_{\mathrm{i}}=\frac{1}{2}n_{\mathrm{i}}\sqrt{\frac{8k_{\mathrm{B}}T_{\mathrm{i}}}{\pi m_{\mathrm{i}}}}+\mu_{\mathrm{i}}n_{\mathrm{i}}(\boldsymbol{n}\cdot\boldsymbol{E}_0), \tag{13}$$

$$\boldsymbol{n}\cdot\boldsymbol{\Gamma}_{\mathrm{k}}=\frac{1}{2}n_{\mathrm{k}}\sqrt{\frac{8k_{\mathrm{B}}T_{\mathrm{k}}}{\pi m_{\mathrm{k}}}}, \tag{14}$$

where T_{i} (T_{k}) and m_{i} (m_{k}) are the ion temperature (neutral particle temperature) and ion mass (neutral particle mass), and k_{B} is the Boltzmann constant.

The Poisson's equation is used to solve electrostatic field

$$\nabla^2V_0=-\frac{\rho_{\mathrm{V}}}{\varepsilon_0}, \tag{15}$$

$$\boldsymbol{E}_0=-\nabla V_0, \tag{16}$$

where ρ_{V} is the charge density, ε_0 is the vacuum permittivity, and V_0 is the electric potential. Since the walls of the chamber are grounded, the boundary conditions for the electric potential is $V_0=0$.

The neutral particles included in this model are H_2, H, H^*, H^{**}, Ar, Ar^* and the charged particles included are electron, H^+, H_2^+, H_3^+, Ar^+, and ArH^+. Reactions for H_2 plasma are listed in Table 1, reactions for Ar plasma are listed in Table 2, and reactions containing both Ar and H_2 are listed in Table 3.

Table 1. Reactions of H_2 plasma included in this work.

Reaction	Rate coefficient ($m^3 \cdot s^{-1}$)	References
1. $e + H_2 \rightarrow e + H_2$	*a*	[39]
2. $e + H \rightarrow e + H$	*a*	[39]
3. $e + H_2 \rightarrow 2e + H + H^+$	*a*	[40]
4. $e + H_2 \rightarrow 2e + H_2^+$	*a*	[40]
5. $e + H_2 \rightarrow e + H + H$	*a*	[41]
6. $e + H_2 \rightarrow e + H + H^*$	*a*, *b*	[42]
7. $e + H \rightarrow 2e + H^+$	*a*	[40]
8. $e + H \rightarrow e + H^*(H^{**})$	*a*, *b*	[40]
9. $e + H^*(H^{**}) \rightarrow 2e + H^+$	*a*, *b*	[40]
10. $e + H_2^+ \rightarrow e + H^+ + H$	*a*	[40]
11. $e + H_2^+ \rightarrow e + H^+ + H^*$	*a*, *b*	[42]
12. $e + H_2^+ \rightarrow H + H$	*a*	[27]
13. $e + H_3^+ \rightarrow e + 2H + H^+$	*a*	[42]
14. $e + H_3^+ \rightarrow 3H$	*a*	[27]
15. $e + H_2^+ \rightarrow 2e + 2H^+$	*a*	[40]
16. $H_2^+ + H_2 \rightarrow H_3^+ + H$	2.11×10^{-15}	[43]

[a]The rate coefficient is obtained by integrating the cross section.
[b]H^* and H^{**} represent the excited states of the hydrogen atom.

Table 2. Reactions of Ar plasma included in this work.

Reaction	Rate coefficient ($m^3 \cdot s^{-1}$)	References
1. $e + Ar \rightarrow e + Ar$	*a*	[44]
2. $e + Ar \rightarrow e + Ar^*$	*a*, *b*	[44]
3. $e + Ar^* \rightarrow e + Ar$	*a*, *b*	[44]
4. $e + Ar \rightarrow 2e + Ar^+$	*a*	[44]
5. $e + Ar^* \rightarrow 2e + Ar^+$	*a*, *b*	[44]
6. $Ar^* + Ar^* \rightarrow e + Ar + Ar^+$	6.4×10^{-16}	[45]
7. $Ar + Ar^* \rightarrow Ar + Ar$	2.3×10^{21}	[45]

[a]The rate coefficient is obtained by integrating the cross section.
[b]Ar^* represent the excited states of the Ar.

Table 3. Reactions between Ar and H_2 included in this work.

Reaction	Rate coefficient ($m^3 \cdot s^{-1}$)	References
1. $H_2^+ + Ar \rightarrow H + ArH^+$	2.3×10^{-15}	[27]
2. $H_3^+ + Ar \rightarrow H_2 + ArH^+$	1×10^{-17}	[27]
3. $H_2 + Ar^+ \rightarrow H + ArH^+$	7.4×10^{-16}	[27]
4. $e + ArH^+ \rightarrow H + Ar$	1×10^{-13}	[27]
5. $H_2 + Ar^+ \rightarrow H_2^+ + Ar$	2.1×10^{-16}	[27]
6. $H_2 + ArH^+ \rightarrow H_3^+ + Ar$	1.5×10^{-15}	[27]
7. $H_2^+ + Ar \rightarrow H_2 + Ar^+$	2.2×10^{-16}	[27]

The magnetic field module is used to solve the power absorption density. By introducing the magnetic vector potential and considering the harmonic approximation ($\boldsymbol{A} = \boldsymbol{A}_1 e^{i\omega t}$), Maxwell's equations yield

$$\left(i\omega\sigma - \omega^2\varepsilon\right)\boldsymbol{A}_1 + \nabla \times \left((\mu)^{-1}\nabla \times \boldsymbol{A}_1\right) = \boldsymbol{J}_{\text{coil}}, \quad (17)$$

where $\boldsymbol{A}_1$ is the amplitude value, ω is the angular frequency, σ is the conductivity, ε is the dielectric constant, μ is the magnetic permeability, i is the imaginary unit, and $\boldsymbol{J}_{\text{coil}}$ is the coil current density.

The power absorption density is

$$P_{\text{abs}} = \frac{1}{2}\text{Re}\left(\boldsymbol{E}_1^* \cdot \boldsymbol{J}_{\text{p}}\right), \quad (18)$$

where $\boldsymbol{E}_1 = i\omega\boldsymbol{A}_1$ is the inductive electric field and $\boldsymbol{J}_{\text{p}} = \sigma \cdot \boldsymbol{E}_1$ is the plasma current density.

The inductive electric field have a zero tangential component at the boundaries.

4. Results and discussion

4.1. Electrical parameter measurement in the driver region

The evolutions of electron density n_e and effective electron temperature T_{eff} with increasing Ar fraction under different pressures at $z = 6$ cm and 2 kW are shown in Fig. 2. It can be seen that the n_e increases markedly with the f_{Ar} when the f_{Ar} lower than 5%–10% at 0.3 Pa, where f_{Ar} is the Ar fraction. As f_{Ar} higher than 10%, the n_e gradually increases with the increasing f_{Ar}. However, the marked increase in n_e with increasing f_{Ar} will disappear when the total pressure rises. At the pressure measured in the experiment, n_e increases by a factor 10–12 as the discharge changes from hydrogen to argon, and it shows a good agreement with the previous studies.[24,26,28] The measured effective electron temperature has an abrupt decrease with increasing f_{Ar} until it reaches 10%, and then T_{eff} remains flat with the increase of f_{Ar} at 0.3 Pa. As the total pressure increases, the phenomenon of T_{eff} abruptly decreasing disappears, and the T_{eff} nearly constant or slightly decrease with the increasing f_{Ar}.

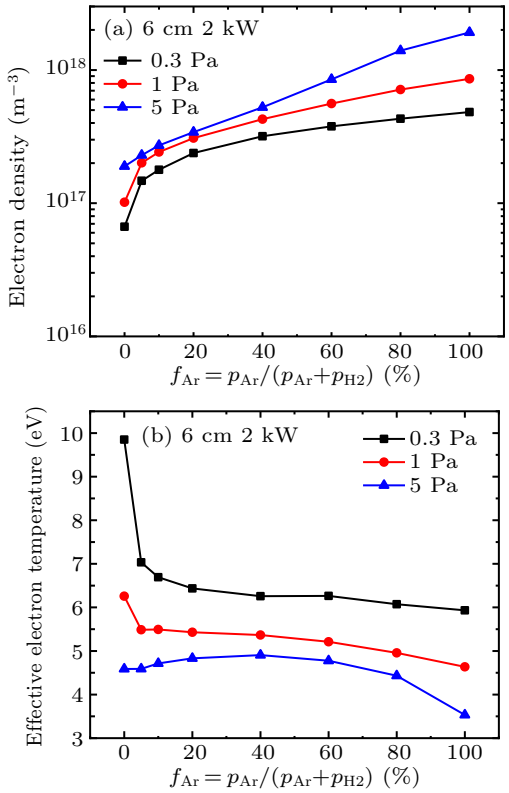


Fig. 2. (a) Electron density and (b) effective electron temperature *versus* Ar fraction at $z = 6$ cm.

Figure 3(a) shows the measured EEPFs at various f_{Ar} at 0.3 Pa and $r = 6$ cm. It can be seen that the EEPF presents a

three-temperature structure with a well-expressed low energy bump and a fall in the high energy electron tail in pure hydrogen discharge. A small amount of argon mixing (5%) makes the low energy electron group increase markedly, while the high energy tail decreases significantly, and the EEPF evolves into a bi-Maxwellian-type distribution which are separated by a kink. As the f_{Ar} continues to increase, the kink appears to move towards the high-energy region as observed by Kimura and Kasugai.[26]

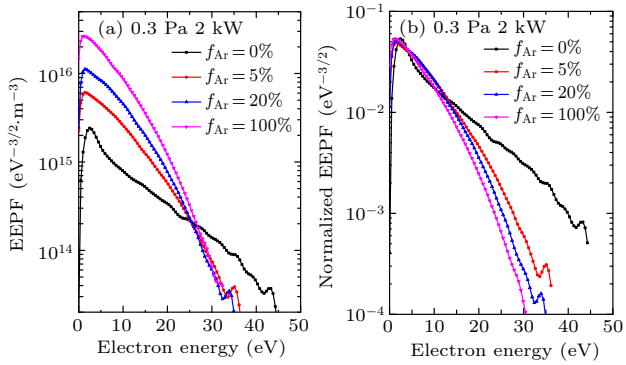


Fig. 3. The measured (a) EEPFs and (b) normalized EEPFs as a function of the electron energy under different Ar fractions at 0.3 Pa and $z = 6$ cm.

The normalized EEPFs are shown in Fig. 3(b) for demonstrating the ratios of the low energy and high energy electron groups to the total electron density. The three-temperature structure of EEPF is typical for the non-local electron kinetics in low-pressure at RF discharge. At 0.3 Pa, the RF power absorption by the plasma is dominated by the stochastic heating, which occurs in the skin layer in the vicinity of the antenna coil. Due to the trapped of the ambipolar potential inherent to bounded plasma, low energy electrons cannot arrive in the skin layer to participate in the heating process, which leads to a well-expressed low energy bump in EEPF. The inelastic collision processes participated by high energy electrons contribute to the fall in the high energy electron tail of EEPF. Thus, the EEPF presents a three-temperature structure in pure hydrogen discharge at 0.3 Pa. As a small amount of argon mixing, the mixed argon atom induces more generation of electrons, by means of its larger impact cross section and smaller ionization threshold energy. Therefore, the high energy electrons are depleted due to the electron impact ionization, meanwhile, a great quantity of low energy electrons are generated. Additionally, increasing electron density raises the frequency of e–e collisions, which may responsible for Maxwellization of the low energy part of EEPF. Consequently, the EEPF shape at 6 cm changes from the three-temperature structure in pure hydrogen discharge to the bi-Maxwellian distribution which are separated by a kink in H_2/Ar discharge. And this process is accompanied by the rapid change of electron density and electron temperature as shown in Fig. 2. The kink in EEPF shifts towards the high-energy region as the f_{Ar} continue increases, which is linked to the change of the lowest excitation threshold energy, as considered by Kimura and Kasugai.[26]

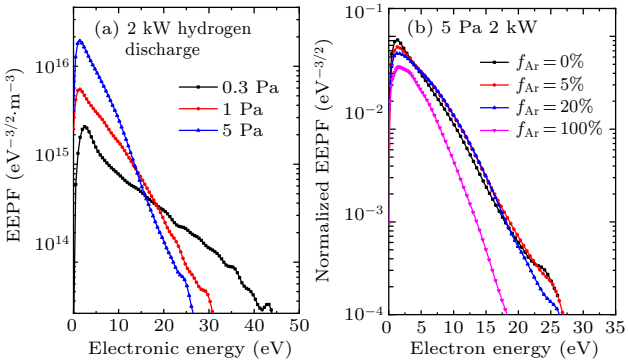


Fig. 4. The measured normalized EEPFs at $z = 6$ cm (a) under different pressures in hydrogen plasma and (b) under different Ar fractions at 5 Pa.

In order to better understand the effect of gas ratio on EEPF at high pressure, figure 4(a) first shows the EEPFs under different pressures in pure hydrogen discharge at 6 cm. As one can see, the high energy electron tail decreases rapidly with the increase of pressure, and the EEPF shape evolves from the three-temperature structure to Maxwellian distribution as expected. The electron heating mechanism growing with gas pressure changes from the stochastic heating dominated to the Ohmic heating dominated.[36] At this time, the low energy electron can obtain energy by electron–neutral collisions from the electric field at the bulk plasma. Meanwhile, the e–e collisions proportional to $n_{\mathrm{e}}\varepsilon^{3/2}$ are increase with increasing gas pressure, and this collisions 'Maxwellianized' the low energy electron.[46] Therefore, the EEPF evolves into Maxwellian distribution with growth of pressure. When the pressure is 5 Pa, a small amount of argon mixing has no obvious effect on normalized EEPF as one can see in Fig. 4(b), since the newly generated electrons 'Maxwellianized' by the way mentioned above. Thus, the effective temperature is nearly constant with the increasing f_{Ar} at 5 Pa.

4.2. Electrical parameter measurement in the expansion region

In this subsection, we give the variation of electrical parameters in the expansion region under the same conditions to observe the difference from the driver region due to the change of spatial location. The electron density and the effective electron temperature as a function of f_{Ar} under different pressures at $z = 24$ cm are shown in Fig. 5. It can be seen that the variation trend of electron density with increasing f_{Ar} at 0.3 Pa is similar to that in the driver region, that is, the electron density first increases markedly when the f_{Ar} lower than 5%–10% and then linearly increases. However, at 5 Pa, the electron density increases slowly or nearly constant with the f_{Ar} when the f_{Ar} is lower than 60%, and there is a rapidly increase of the electron

density by about 30 times when the discharge changes from mixed gas to pure argon. The effective temperature is nearly constant or slightly increases with the rising f_{Ar} at different pressures, and its variation amplitude does not exceed 1 eV.

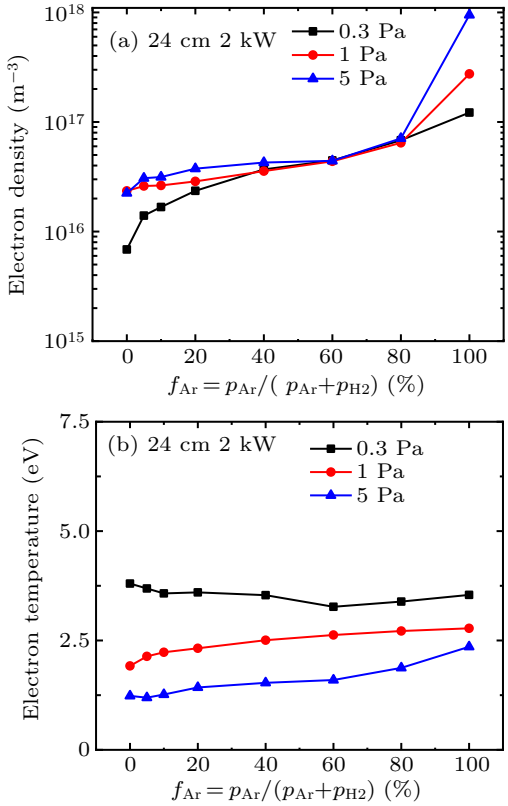


Fig. 5. (a) The electron density and (b) the effective electron temperature *versus* Ar fraction at $z = 24$ cm.

Figure 6(a) shows the EEPFs as a function of the electron kinetic energy at different f_{Ar} at 0.3 Pa and $z = 24$ cm. It is found that the EEPF appears to be a Maxwellian distribution in hydrogen discharge, and adding Ar does not change its shape. Moreover, with the increase of f_{Ar}, the low energy electron and the high energy groups exhibit a considerable increase. Electron diffusion is the primary factor affecting the electrical parameters in the expansion region, since electrons cannot obtain energy in this region. The electron energy relaxation length calculated by COMSOL is approximately 50.8 cm–61.9 cm in hydrogen discharge at 0.3 Pa experimental condition, whereas it ranges from 59 cm to 324 cm in argon discharge. Since the measurement range of Langmuir probe is smaller than the electron energy relaxation, the electron nonlocal kinetics is satisfied. Therefore, the electrons heated in the driver region can be transported to the measurement position in the expansion region without inelastic collision, and the EEPF as a function of the total energy (equals to the sum of the electron kinetic energy and the potential energy) is spatially uniform. As shown in Figs. 6(b)–6(e), the EEPFs as a function of the total energy are coincident with that at 6 cm in different Ar ratios except for the cutting of the low energy electrons as expected, which is typical for the nonlocal kinetics. The cutting energy is the electron potential energy, and it is the difference between the plasma potential at 24 cm and the discharge center 6 cm. It is the reason why the variation of electron density and electron temperature with increasing f_{Ar} is similar to that of the driver region at 0.3 Pa. Since the electrons with energies above the ambipolar dc potential can transport to the measurement position in the expansion region, the EEPFs are cut in low energy range. It should be noted that the cutting of the low energy electrons in the EEPFs decreases with the increasing f_{Ar}, which means that the ambipolar potential between the two measuring positions decreases. Due to the velocity of the electrons is faster, ions need to acquire energy in a bipolar potential field for acceleration in order to maintain quasi-neutrality of the plasma. With the addition of argon, the effective electron temperature decreases in the driver region as the high energy electrons lose kinetic energy through ionization reactions, meanwhile, the energy required for ions to accelerate in an ambipolar field to meet the quasi-neutral condition of plasma is reduced.

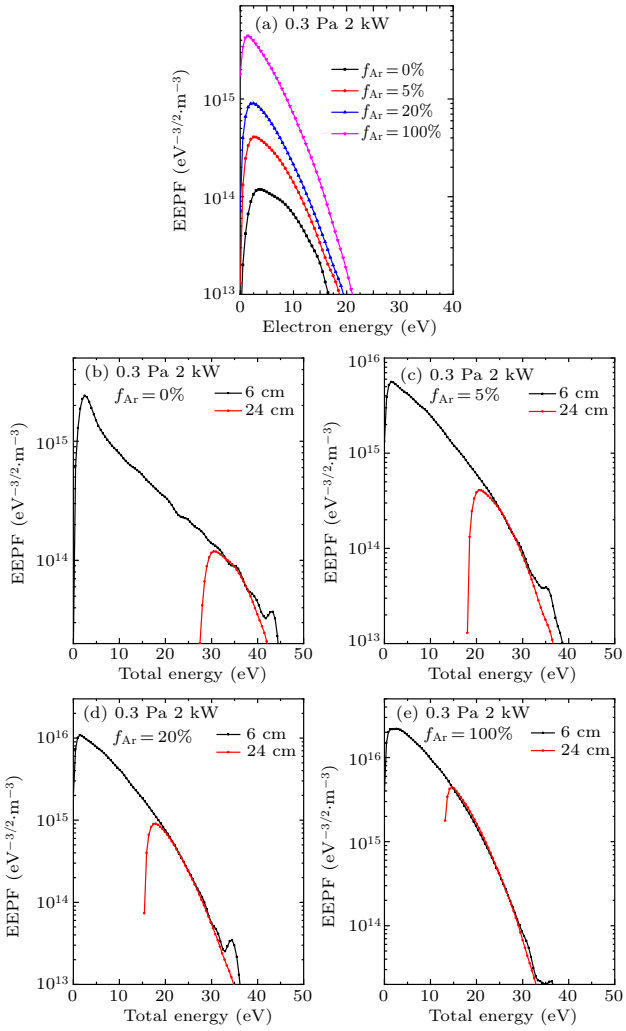


Fig. 6. (a) The measured EEPFs as a function of electron energy at $z = 24$ cm. (b)–(e) EEPFs as a function of total electron energy at $z = 6$ cm and $z = 24$ cm under different Ar fractions.

In Fig. 7(a), the normalized EEPFs at different pressures during pure hydrogen discharge are shown. As pressure increases, the Maxwellian EEPFs at low pressure (0.3 Pa) transition into bi-Maxwellian-type distribution with pronounced low energy electrons. This change of EEPFs with pressure in hydrogen discharge has been studied by Abdel-Fattah[47] in a CCP discharge and Krištof *et al.*[48] in an ICP discharge. According to Abdel-Fattah *et al.*, the enhancement of molecular vibrational excitation or dissociation of negative hydrogen ions is the reason for the change in EEPF shape with pressure. Fewer negative hydrogen ions present through the volume process suggest that the vibrational excitation reaction of hydrogen molecules in the electron transport process is the reason for the formation of the bi-Maxwellian distribution of EEPF. The calculation shows that the electron energy relaxation length is about 6.1 cm–28.9 cm under the experimental condition of 5 Pa in hydrogen discharge, which is smaller than the measurement range of Langmuir probe. Therefore, the nonlocal condition is not met, that is, the electrons heated in the driver region will undergo inelastic collision when they move towards the expansion region.

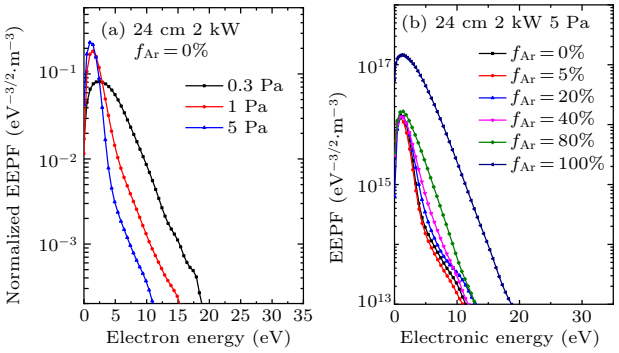


Fig. 7. The measured (a) normalized EEPFs at different pressures in hydrogen plasma, (b) EEPFs at different Ar fractions in 5 Pa, at $z = 24$ cm.

In order to demonstrate the variation of EEPF with f_{Ar} at 5 Pa, figure 7(b) shows a relatively large number of measurement results. It can be seen that EEPFs gradually evolve from a bi-Maxwellian distribution with pronounced lower energy electrons to a Maxwellian distribution as the increasing f_{Ar} when the f_{Ar} is below 80%, and both the low energy electron and the high energy groups show a significant increase as the f_{Ar} further increases. The vibrational excitation reaction of hydrogen molecules in the electron transport process decreases as the f_{Ar} increases, leading to a reduction in the low energy electrons produced by the vibrational excitation reaction of high energy electrons, which makes the shape of the EEPF becomes a Maxwellian. However, when the f_{Ar} is lower than 80%, there are still a significant amount of inelastic collision. These inelastic collisions prevent the energetic electrons generated in the driver region overcoming the ambipolar potential well, thus the electron density is slightly increases with the increasing f_{Ar} in H_2/Ar mixed discharge. Due to the disappearance of molecular reactions and the electron's longer energy relaxation length (approximately 26.9 cm–581 cm under the experimental condition in argon discharge), the electrons can diffuse to further locations in argon discharge. Therefore, the electron density has a rapidly increase when the discharge changes from mixed gas to pure argon. As the effective electron temperature is obtained via integrals of the EEPF, it has little variation with the increasing f_{Ar}.

4.3. Validation of experiment and simulation

In order to better understand the characteristics of plasma and verify the experimental results, we have provided simulation results and compared them with experimental results. Figure 8 illustrates the two-dimensional (2D) distributions of the calculated electron density and effective electron temperature for different f_{Ar} at 0.6 Pa. For all f_{Ar}, the electron density peaks in the driver region center where the ionization rate is maximum. And, the effective electron temperature maximum at the side wall, closes the skin layer in the vicinity of the antenna coil.

For a more intuitive comparison between experimental and simulation results, figure 9 demonstrates the variation of the electron density and the effective electron temperature with pressure for different f_{Ar} at 6 cm. It is obvious that the electron density exhibits an initial increase followed by stabilization or slight growth with the increase of pressure for all f_{Ar} at 6 cm as shown in Fig. 9(a). At the same time, the effective electron temperature shows an opposite trend with pressure, decreasing initially and stabilizing thereafter, in Fig. 9(b). Furthermore, the effective temperature of hydrogen discharge experiences a larger decrease compared to argon-containing plasma, with an amplitude of approximately 5 eV, compared to approximately 1.5 eV–2.5 eV in argon-containing plasma. This is because hydrogen molecules contain more plasma chemistry, which involves a variety of vibrational excitation reactions, then the high-energy electrons will be consumed significantly due to the increase of inelastic collision as the pressure increases. Therefore, the effective electron temperature of hydrogen discharge decreases obviously with increasing pressure. A small amount of argon mixing can cause a significant consumption of high-energy electrons at low pressure as mentioned above, so the influence of pressure on effective electron temperature in argon-containing plasma is decreased. Figures 9(c) and 9(d) show the calculated electron density and the effective electron temperature with pressure for different f_{Ar}. It can be seen that the variation of calculated electron density and effective electron temperature with pressure are similar to those in the experiment for all f_{Ar}. Specifically, the electron density initially increases, followed by stabilization or slight growth as pressure increases, regardless f_{Ar}. Moreover, the effective temperature of hydrogen discharge exhibits a more significant decrease compared to the argon-containing plasma. It should be noted, however, that there is a disparity between the absolute values obtained from the calculations and those obtained from the experiment. This is due to the presence of power coupling efficiencies experimentally, whereas the simulation uses the

full 2-kW power. In addition, the EEPFs are Maxwellian distribution in the model under any discharge parameter, which is inaccurate as can be seen from the above experimental results. The use of experimentally measured power coupling efficiencies and EEPFs in the model might optimize the difference in values.

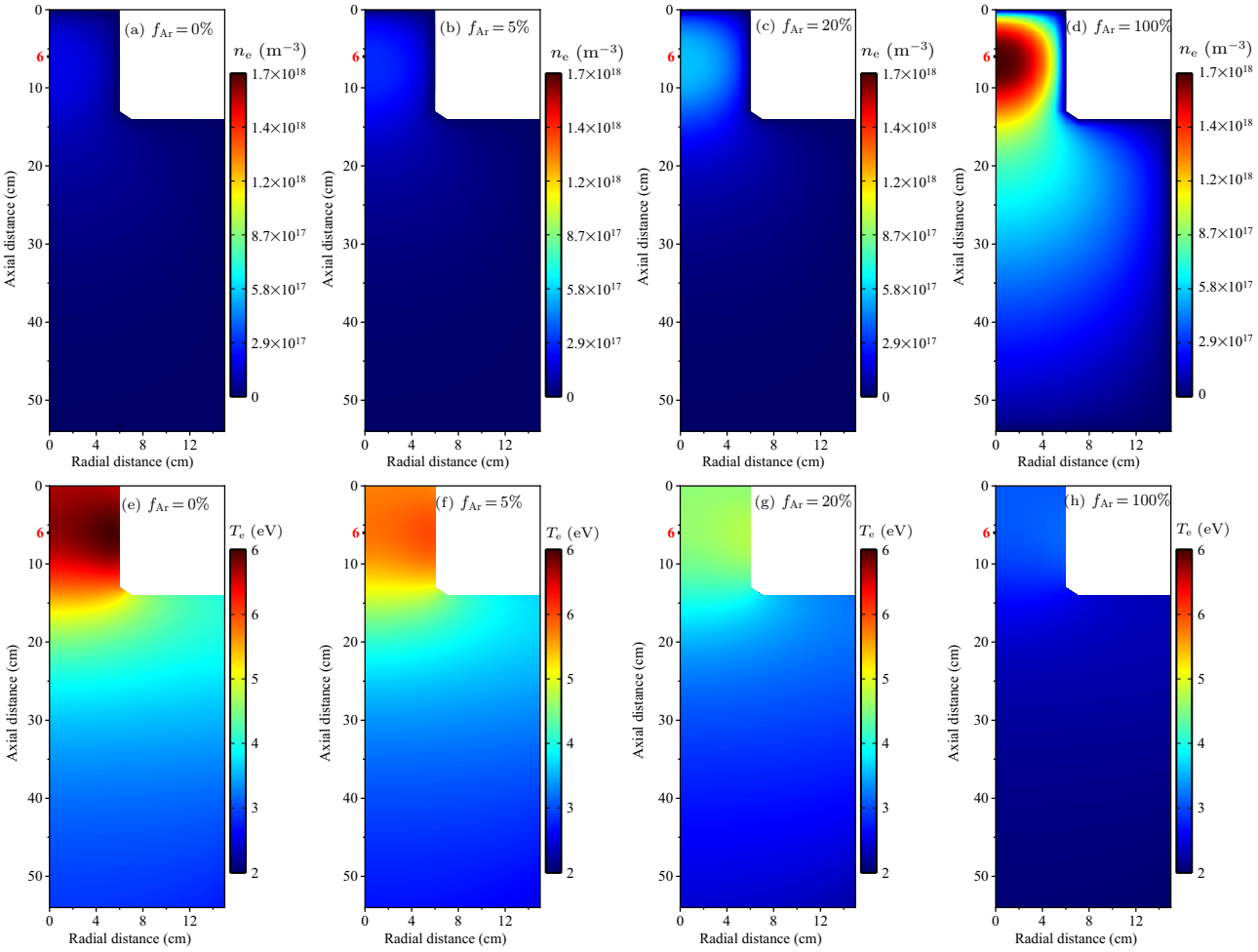


Fig. 8. The 2D distribution of electron density (a)–(d) and the electron temperature (e)–(h) in simulation at 0.6 Pa for different Ar fractions.

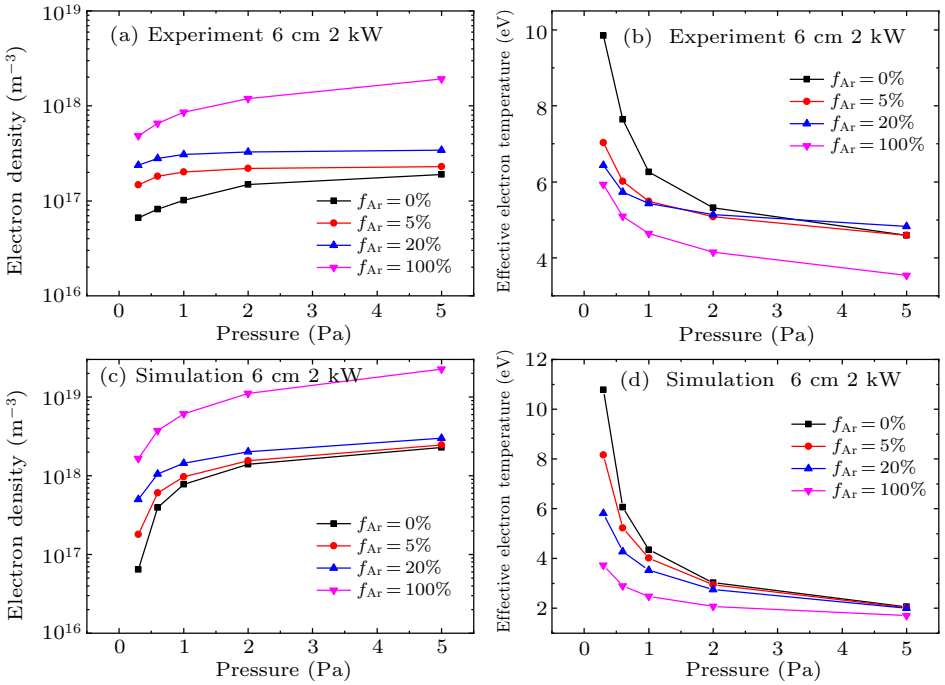


Fig. 9. The electron density [(a) and (c)] and effective electron temperature [(b) and (d)] obtained by experiment (up) and simulation (down) *versus* pressure at 6 cm and 2 kW under different Ar fractions.

The experimentally measured axial profiles of electron density and effective electron temperature for different f_{Ar} at 0.6 Pa are present in Figs. 10(a) and 10(b). The electron density distributions are unimodal for all f_{Ar}, which is consistent with the previous studies. With the increase of f_{Ar}, the electron density in the driver region, which is the main areas where the ionization reactions occur, becomes more pronounced. The effective electron temperature exhibits a peak at the 6 cm, and then decreases towards both sides of the chamber, consistent with previous findings for all f_{Ar}. Additionally, the effective electron temperature shows a significant decrease in most regions of the chamber when a small amount of argon (5%) is introduced. Furthermore, when the f_{Ar} continues to increase, the magnitude of the effective electron temperature change is relatively small, as explained in the previous section. The calculated electron density and the effective electron temperature by COMSOL software are shown in Figs. 10(c) and 10(d). The variation of calculated electron density and effective electron temperature with axial position are similar to that observed in the experiment with a maximum at the center of driver region and a decrease towards both sides of the chamber. However, the calculated effective electron temperature shows a significant decrease throughout the entire chamber as f_{Ar} increases. Although this trend seems reasonable, it differs from experimental measurements which may be due to the limited number of reactions taking into considered in the simulations.

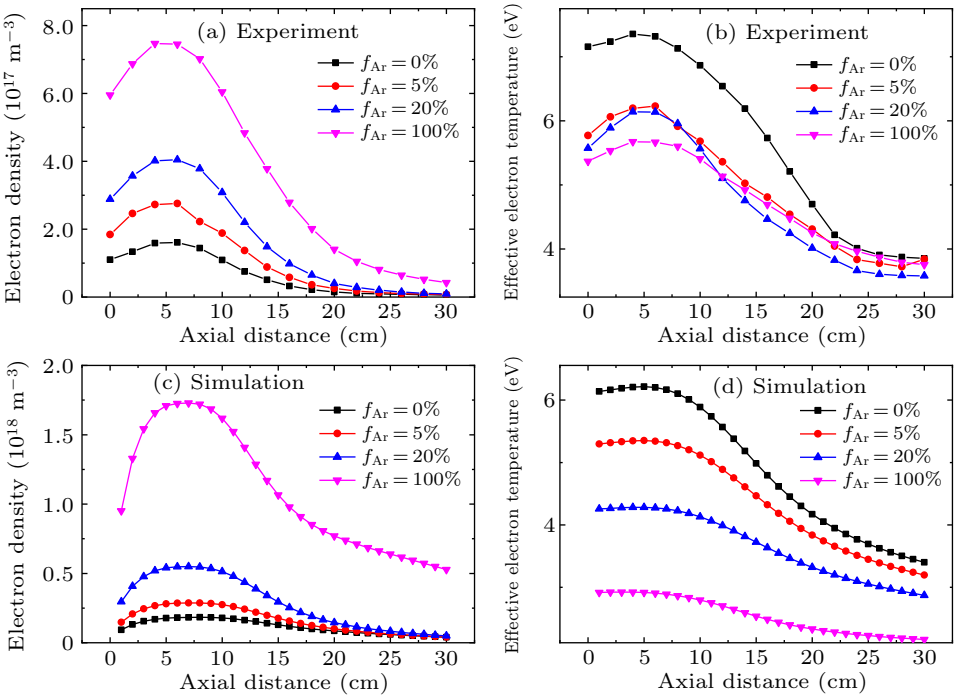


Fig. 10. The axial profiles of electron density [(a) and (c)] and effective electron temperature [(b) and (d)] obtained by experiment (up) and simulation (down) at 0.6 Pa and 2 kW for different Ar fractions.

5. Conclusions

In summary, this study investigates the impact of different mixing ratios on the variation of electrical parameters in a cylindrical inductive H_2/Ar discharge with an expansion region, employing a Langmuir probe for measurement. The measured electron density in the driver region increases with the f_{Ar} under all experimental conditions, attributed to the growing generation mechanism of electrons. It obvious that the addition of a small amount of Ar at low pressure causes a significant depletion of energetic electrons, and the EEPF changes from a three-temperature distribution to a bi-Maxwellian distribution, which is accompanied by a rapid increase of electron density and a decrease of electron temperature. However, the normalized EEPF with a small amount argon mixing at high pressure coincides with that during the hydrogen discharge, as the Ohmic heating of electrons and the e–e collisions play a dominant role in 'Maxwellianized' newly generated electrons.

At low pressure, the electron energy relaxation length exceeds the measured distance. Consequently, the EEPFs of the total electron energy at 24 cm are coincident with those at 6 cm in different f_{Ar}, and the variation of electron density with f_{Ar} is similar to the driver region. With increasing of total pressure, the electron kinetics change from nonlocal to local in hydrogen discharge, which means that the electrons undergo inelastic collisions in the transport process. Thus, the EEPF shape at 24 cm is a bi-Maxwellian distribution with pronounced low energy electrons due to the numerous vibrational excitation reactions in the hydrogen discharge. When the argon fraction increases, the EEPF shape evolves into a Maxwellian distribution. This phenomenon is related to the decrease of hydrogen molecular reactions and the longer electron energy relaxation

length in argon discharge. As the occurrence vibrational excitation reactions and the confinement of the ambipolar potential well, the electron density is nearly constant with the f_{Ar} for the f_{Ar} lower than 60%. Furthermore, we present the variation of experimentally measured electron density and the effective electron temperature with pressure and axial position for different f_{Ar}. The obtained results show a strong agreement with the calculations performed using COMSOL software.

Acknowledgements

Project supported by the National Natural Science Foundation of China (Grant Nos. 11935005 and 12075049) and the National Key Research and Development Program of China (Grant No. 2017YFE0300106).

References

[1] Shul R, Willison C, Bridges M, Han J, Lee J, Pearton S, Abernathy C, MacKenzie J, Donovan S, Zhang L and Lester L 1998 *J. Vac. Sci. Technol. Vac. Surf. Films* **16** 1621
[2] Bae J W, Jeong C H, Kim H K, Kim K K, Cho N G, Seong T Y, Park S J, Adesida I and Yeom G Y 2003 *Jpn. J. Appl. Phys.* **42** L535
[3] Curley G A, Gatilova L, Guilet S, Bouchoule S, Gogna G S, Sirse N, Karkari S and Booth J P 2010 *J. Vac. Sci. Technol. Vac. Surf. Films* **28** 360
[4] Faraz T, Arts K, Karwal S, Knoops H C and Kessels W M 2019 *Plasma Sources Sci. Technol.* **28** 024002
[5] Ye R, Murphy A B and Ishigaki T 2007 *Plasma Chem. Plasma Process.* **27** 189
[6] Tanaka Y 2009 *Thin Solid Films* **518** 936
[7] Banerjee A and Das D 2015 *Appl. Surf. Sci.* **330** 134
[8] Speth E, Falter H, Franzen P, Fantz U, Bandyopadhyay M, Christ S, Encheva A, Fröschle M, Holtum D, Heinemann B, Kraus W, Lorenz A, Martens Ch, McNeely P, Obermayer S, Riedl R, Süss R, Tanga A, Wilhelm R and Wünderlich D 2006 *Nucl. Fusion* **46** S220
[9] Froschle M, Speth E, Falter H, Fantz U, Franzen P, Riedl R, Heinemann B, Kraus W, Martens C, McNeely P, Tanga A, Holtum D and Encheva A 2005 *SOFE* 05, 26–29 September 2005, Knoxville, Tennessee, TN, USA p. 1
[10] Hemsworth R, Decamps H, Graceffa J, Schunke B, Tanaka M, Dremel M, Tanga A, De Esch H, Geli F, Milnes J, Inoue T, Marcuzzi D, Sonato P and Zaccaria P 2009 *Nucl. Fusion* **49** 045006
[11] Franzen P, Falter H, Fantz U, Kraus W, Berger M, Christ-Koch S, Fröschle M, Gutser R, Heinemann B, Hilbert S, Leyer S, Martens C, McNeely P, Riedl R, Speth E and Wünderlich D 2007 *Nucl. Fusion* **47** 264
[12] Heinemann B, Fantz U, Kraus W, Wünderlich D, Bonomo F, Froeschle M, Mario I, Nocentini R, Riedl R and Wimmer C 2018 *Fusion Eng. Des.* **136** 569
[13] Serianni G, Toigo V, Bigi M, Boldrin M, Chitarin G, Dal Bello S, Grando L, Luchetta A, Marcuzzi D, Pasqualotto R and others 2019 *Fusion Eng. Des.* **146** 2539
[14] Fantz U, Bonomo F, Fröschle M, Heinemann B, Hurlbatt A, Kraus W, Schiesko L, Nocentini R, Riedl R and Wimmer C 2019 *Fusion Eng. Des.* **146** 212
[15] Fox-Lyon N, Oehrlein G, Ning N and Graves D 2011 *J. Appl. Phys.* **110** 104314
[16] Moon C S and Han J G 2008 *Thin Solid Films* **516** 6560
[17] Choi J S, Cho D H, Lim E T and Chung C W 2019 *J. Nanosci. Nanotechnol.* **19** 6506
[18] He Y, Su Y, Zhu M, Cao B and Dong B 2012 *Sci. China Phys. Mech. Astron.* **55** 2070
[19] Carazzetti P, Weichart J, Erhart A, Elghazzali M and Strolz E 2020 2020 *IEEE 70th Electronic Components and Technology Conference (ECTC)*, 03–30 June 2020, Orlando, Florida, USA, p. 1711
[20] Das D and Karmakar L 2017 *AIP Conf. Proc.* **1832** 050065
[21] Karmakar L and Das D 2020 *J. Alloys Compd.* **847** 155352
[22] Lim J W M, Huang S, Chan C S, Xu S, Wei D, Guo Y, Xu L and Ostrikov K 2016 *Procedia Eng.* **139** 147
[23] Lim J, Huang S, Xu L, Lim Y, Loh Y, Chan C, Bazaka K, Levchenko I and Xu S 2018 *Sol. Energy* **171** 841
[24] Gudmundsson J T 1998 *Plasma Sources Sci. Technol.* **7** 330
[25] Gudmundsson J T 1999 *Plasma Sources Sci. Technol.* **8** 58
[26] Kimura T and Kasugai H 2010 *J. Appl. Phys.* **107** 083308
[27] Hjartarson A, Thorsteinsson E and Gudmundsson J 2010 *Plasma Sources Sci. Technol.* **19** 065008
[28] Sode M, Schwarz-Selinger T and Jacob W 2013 *J. Appl. Phys.* **114** 063302
[29] Sode M, Schwarz-Selinger T, Jacob W and Kersten H 2014 *J. Appl. Phys.* **116** 013302
[30] Fox-Lyon N, Knoll A, Franek J, Demidov V, Godyak V, Koepke M and Oehrlein G 2013 *J. Phys. Appl. Phys.* **46** 485202
[31] Fox-Lyon N and Oehrlein G S 2014 *J. Vac. Sci. Technol. B* **32** 041206
[32] Huh S R, Kim N K, Jung B K, Chung K J, Hwang Y S and Kim G H 2015 *Phys. Plasmas* **22** 033506
[33] Yang W, Li H, Gao F and Wang Y N 2018 *Plasma Sources Sci. Technol.* **27** 075006
[34] Gao F, Zhang Y R, Li H, Liu Y and Wang Y N 2017 *Phys. Plasmas* **24** 073508
[35] Li H, Liu Y, Zhang Y R, Gao F and Wang Y N 2017 *J. Appl. Phys.* **121** 233302
[36] Gao F, Li H, Yang W, Liu J, Zhang Y R and Wang Y N 2018 *Phys. Plasmas* **25** 013515
[37] Li H, Gao F, Wen D Q, Yang W, Du P C and Wang Y N 2019 *J. Appl. Phys.* **125** 173303
[38] Lieberman M A and Lichtenberg A J 2005 *Principles of Plasma Discharges and Materials Processing*, 2nd edn. (New York: Wiley)
[39] Petrov G and Giuliani J 2001 *J. Appl. Phys.* **90** 619
[40] Janev R K, Reiter D and Samm U 2003 *Collision processes in low-temperature hydrogen plasmas* (Forschungszentrum Jülich: Zentralbibliothek)
[41] Yoon J S, Song M Y, Han J M, Hwang S H, Chang W S, Lee B and Itikawa Y 2008 *J. Phys. Chem. Ref. Data* **37** 913
[42] Janev R K, Langer W D, Evans K and Post D E 1987 *Elementary Processes in Hydrogen-Helium Plasmas– Cross Sections and Reaction Rate Coefficients* (Berlin: Springer-Verlag)
[43] Bowers M, Elleman D and King Jr J 1969 *J. Chem. Phys.* **50** 4787
[44] Kudryavtsev A and Serditov K Y 2012 *Phys. Plasmas* **19** 073504
[45] Bogaerts A and Gijbels R 1995 *Phys. Rev. A* **52** 3743
[46] Godyak V A, Piejak R and Alexandrovich B 2002 *Plasma Sources Sci. Technol.* **11** 525
[47] Abdel-Fattah E and Sugai H 2013 *Phys. Plasmas* **20** 023501
[48] Krištof J, Annušová A, Anguš M, Veis P, Yang X, Angot T, Roubin P and Cartry G 2016 *Phys. Scr.* **91** 074009